

Additive Manufacturing of Biomechanically Tailored Meshes for Compliant Wearable and Implantable Devices

Sebastian W. Pattinson,* Meghan E. Huber, Sanha Kim, Jongwoo Lee, Sarah Grunsfeld, Ricardo Roberts, Gregory Dreifus, Christoph Meier, Lei Liu, Neville Hogan, and A. John Hart*

Additive manufacturing (AM) of medical devices such as orthopedic implants and hearing aids is highly attractive because of the potential of AM to match the complex form and mechanics of individual human bodies. Externally worn and implantable tissue-support devices, such as ankle or knee braces, and hernia repair mesh, offer a new opportunity for AM to mimic tissue-like mechanics and improve both patient outcomes and comfort. Here, it is demonstrated how explicit programming of the toolpath in an extrusion AM process can enable new, flexible mesh materials having digitally tailored mechanical properties and geometry. Meshes are fabricated by extrusion of thermoplastics, optionally with continuous fiber reinforcement, using a continuous toolpath that tailors the elasticity of unit cells of the mesh via incorporation of slack and modulation of filament–filament bonding. It is shown how the tensile mesh mechanics can be engineered to match the non-linear response of muscle. An ankle brace with directionally specific inversion stiffness arising from embedded mesh is validated, and further concepts for 3D mesh devices are prototyped.

devices, including orthopedic implants,^[2] orthodontic aligners,^[3] bone scaffolds,^[4] and prostheses.^[5] However, importantly, all of these AM-enhanced devices interface with rigid parts of the body, whereas soft tissues also often require mechanical support to prevent or heal injury.^[6]

The mechanical characteristics of soft tissue support devices are critical to their performance. For example, conventionally manufactured ankle braces, which restrict movement to prevent (re)injury can be bulky and poorly fitting. Implanted surgical mesh, which mechanically supports tissue as it heals following surgery and is used in many of the estimated 20 million hernia surgeries around the world every year,^[7] can restrict abdominal wall mobility and lead to rigidity and discomfort.^[8] These support devices could similarly benefit from the customization and complex geometries enabled by AM.

1. Introduction

Additive manufacturing (AM) enables the digitally driven production of objects that are both individually customized and geometrically complex.^[1] Considering the diversity and complexity of human bodies, AM is therefore well-suited to production of wearable and implantable devices that offer enhanced performance or fit, including by customization, when compared to alternative fabrication methods. These advantages have already led to numerous additively manufactured medical

Producing devices that replicate the mechanics of soft tissues is challenging, though, because tissues such as muscle, tendons, and ligaments often have nonlinear tensile stress–strain responses, with an initially low stiffness that increases rapidly as the tissue becomes taut.^[9] The mechanical response of tissue is also highly anisotropic, varies significantly according to the tissue type, and can be different for individual patients according to their body type and health condition.^[10] For instance, the tensile modulus of rat muscular tissue has been measured to be ≈ 0.1 MPa until a strain of 20%, and

Dr. S. W. Pattinson, Dr. M. E. Huber, Dr. S. Kim, J. Lee, S. Grunsfeld, Dr. R. Roberts, G. Dreifus, Dr. C. Meier, Dr. L. Liu, Prof. N. Hogan, Prof. A. J. Hart
Department of Mechanical Engineering
Massachusetts Institute of Technology
Cambridge, MA 02139, USA
E-mail: swp29@cam.ac.uk; ajhart@mit.edu


Dr. S. W. Pattinson
Department of Engineering
University of Cambridge
Cambridge CB2 1PZ, UK

Dr. S. Kim
Department of Mechanical Engineering
Korea Advanced Institute of Science and Technology
Daejeon 34141, South Korea

S. Grunsfeld
Department of Materials Science and Engineering
Massachusetts Institute of Technology
Cambridge, MA 02139, USA

Dr. R. Roberts
School of Engineering and Sciences
Tecnologico de Monterrey
64849, Mexico

Prof. N. Hogan
Department of Brain and Cognitive Sciences
Massachusetts Institute of Technology
Cambridge, MA 02139, USA

 The ORCID identification number(s) for the author(s) of this article can be found under <https://doi.org/10.1002/adfm.201901815>.

DOI: 10.1002/adfm.201901815

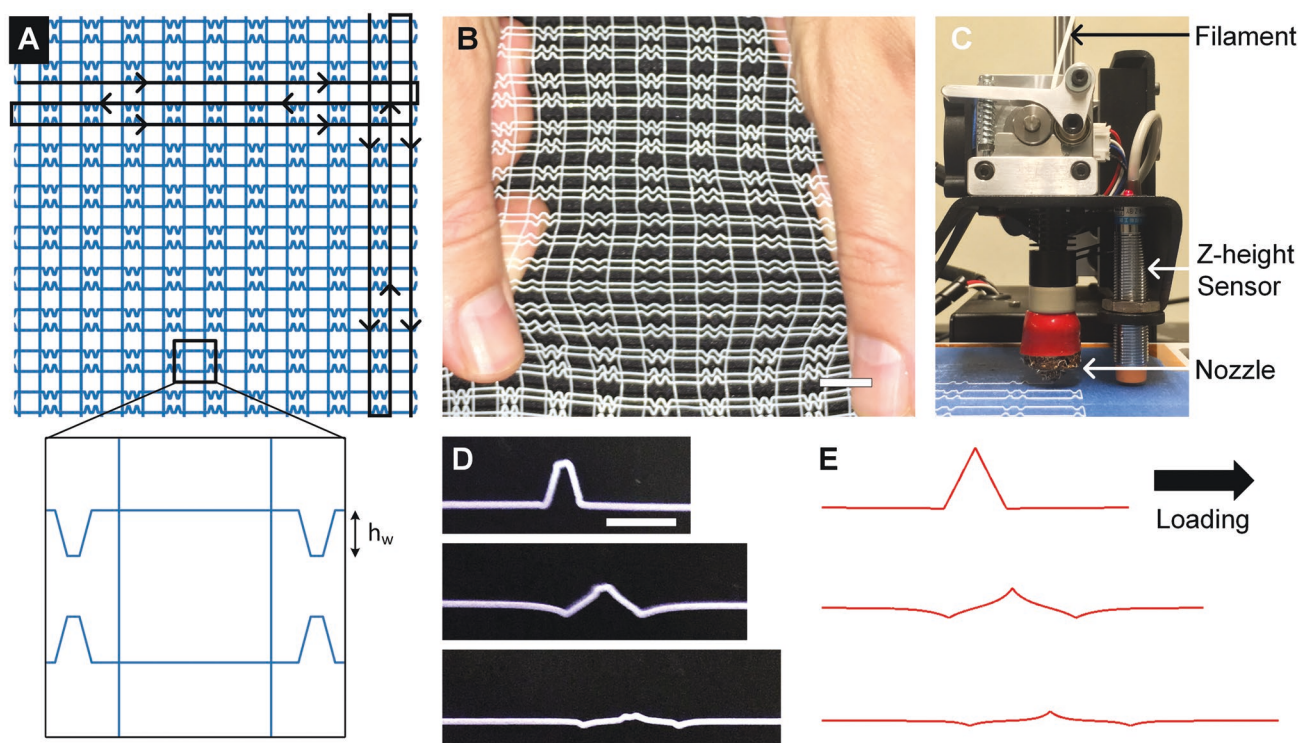


Figure 1. A) Schematic of hierarchical mesh fabrication approach with black lines indicating toolpath; h_w indicates the wave height. B) Exemplary printed mesh (scale bar 10 mm). C) Extruder setup used for mesh printing. D) Image of printed fiber with a wave (scale bar 5 mm), with increasing tensile strain from top to bottom. E) Finite element simulations of an individual fiber with a wave, with increasing tensile strain from top to bottom.

≈ 2.6 MPa beyond 40% strain; for connective tissue the relevant values are ≈ 3 MPa to 10% strain and ≈ 40 MPa thereafter.^[9] These tissues are found in close proximity to one another, meaning that the overall mechanical properties have spatially varying mechanics in addition to significant anisotropy. Additionally, soft tissue support devices should be sufficiently porous to enable breathability (in the case of an external device) or tissue integration (in the case of an implant).

Established methods to produce soft-tissue devices such as wearable braces and implantable mesh typically use conventional fabrics made by knitting or weaving. While there have been exciting innovations in conventional fabrics,^[11–13] weaving is suited to regular patterns and cannot adapt to sharp gradients in mechanical properties, while the looped topologies used in knitting feature limited stiffness and control over 3D structure. Many researchers and designers have explored the utility of AM to produce fabric-like geometries, such as thin, continuous lattice structures or interlocked chainmail.^[14–17] Yet, adaptation of AM to produce soft tissue supports requires detailed consideration of the local and global mechanics necessary to provide meaningful utility as well as design and toolpath planning algorithms capable of adaptation to complex 3D topologies that match the contours of the body.

Here, we present a new, versatile approach to digital fabrication of biomechanically tailored mesh materials using AM. The explicit programming of the toolpath of an extruded thermoplastic, alongside optional reinforcement by continuous fiber, enables the additive manufacturing of meshes with non-linear elasticity to mimic the mechanics and conform to the 3D

structure of soft tissue. We demonstrate the advantages of this method by manufacturing and testing an ankle brace that selectively prevents excessive inversion of the ankle, while leaving the ankle otherwise free to move naturally in all other directions. We show the further possibilities enabled by toolpath control in enhancing the conformity of the meshes to 3D structures by local patterning of Negative Poisson's Ratio structures as well as using nonplanar toolpaths to modulate connectivity and to produce seamless 3D meshes.

2. Results and Discussion

To enable additive manufacturing of meshes with locally varying and anisotropic mechanics, we introduce a hierarchical design where each mesh consists of an array of cells (**Figure 1**). By specifying the mechanical properties of a cell, we specify the local and global mechanics of the mesh. Each cell is composed of orthogonal elements, which determine the tensile response of each cell in its respective direction, and can therefore establish anisotropic response.

Extrusion additive manufacturing, specifically using a thermoplastic elastomer (see the Experimental Section) for demonstration herein, is chosen because of its simplicity and versatility. However, unlike typical extrusion AM implementations where bulk objects are built with rigid bases for attachment to the printer platform, here the mesh is directly printed as one or a few layers, with explicit control of the toolpath to specify the desired mechanical properties of the mesh.

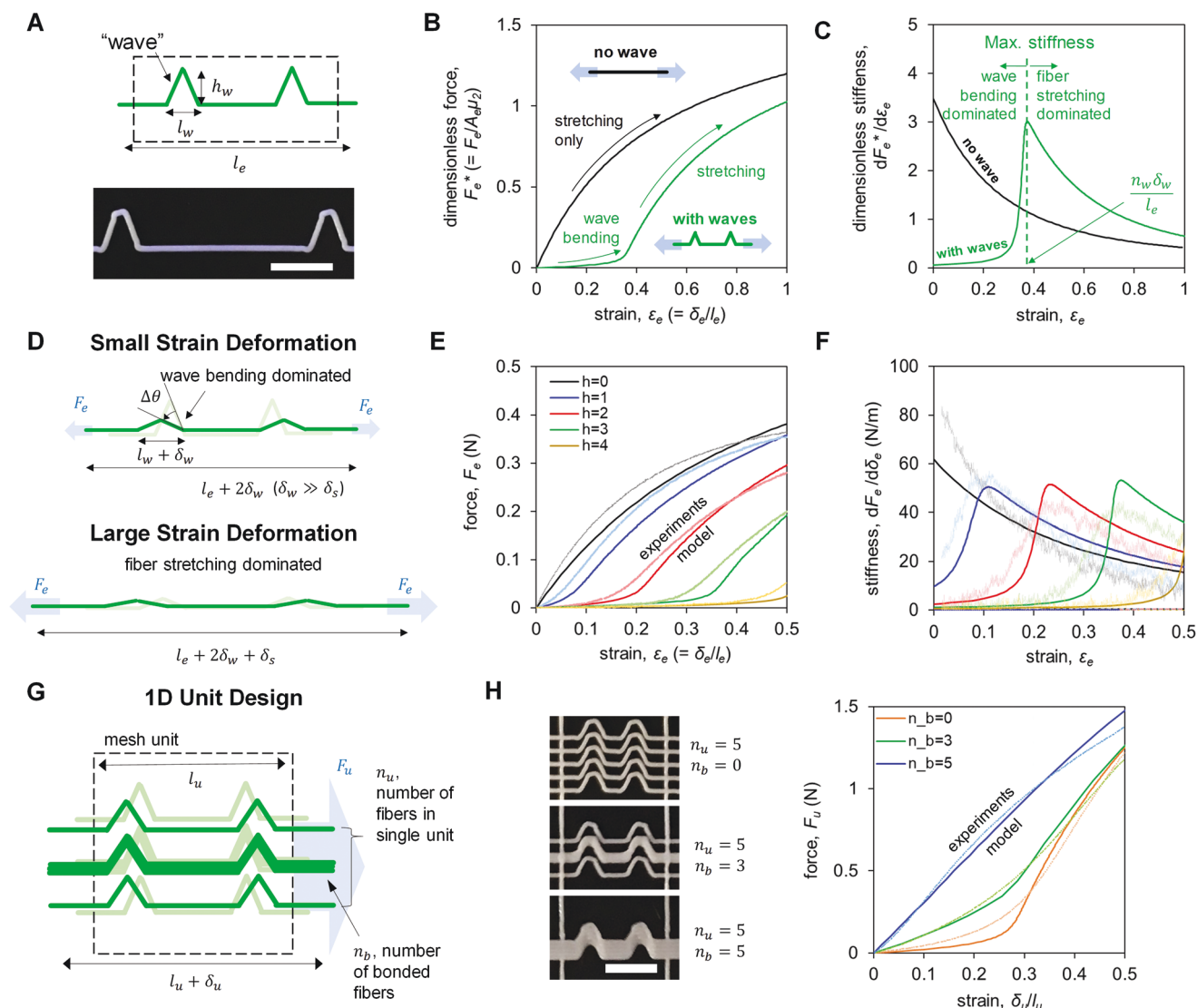


Figure 2. Methods of controlling the nonlinear tensile response of individual fibers (“elements”). A) Schematic and image of fiber waves used to introduce nonlinear behavior (scale bar is 5 mm). B) Mechanical model of tensile response of a fiber with a wave. C) Stiffness of the model fiber in the previous figure. D) Schematic describing the mechanical model. E) Controlling the low-to-high strain transition by varying the wave height. F) Stiffness of the fibers versus strain, for the same parameters as in the previous figure. G) Schematic showing variation in fiber bonding for low strain stiffness modulation. H) Images of three exemplary bonded configurations and corresponding tensile force–displacement curves compared to model.

A continuous toolpath is important for mesh performance because interruptions of the toolpath lead to local defects that can compromise strength and therefore are especially undesirable for medical applications. For meshes where each fiber running vertically or horizontally from one end of the mesh to the other has uniform thickness, the toolpath follows a raster-pattern where all horizontal lines are printed followed by the vertical lines. For meshes where a horizontal or vertical fiber features locally varying thickness, which allows the mesh to exhibit a greater range of local mechanical response, we use the graph theory-based toolpath planning algorithm developed by Dreifus et al.^[18] This algorithm is able to plot complex toolpaths where the extruder passes over each part of the mesh a programmable number of times while minimizing discontinuities. Since the extruder deposits a uniform thickness of thermoplastic each

time it passes over a section of the mesh, this allows for the local control of mesh thickness.

2.1. Engineering Tissue-Like Mesh Mechanics

To create printed mesh that accurately mimics the nonlinear tensile response of soft tissue, we must be able to control the stiffness at small strains (low) and at large strains (high), and the transition strain at which the stiffness significantly increases (Figure 2A,B). For this, we take inspiration from the wavy structure of collagen;^[19] incorporating waves into each fiber segment allows it to be stretched with an effective stiffness initially dominated by bending of the wave, and then subsequently by stretching of the fiber once it is taut. Thus, for

a single segment with two waves and a total projected length l_e , the axial stiffness can be tuned by varying wave amplitude (h_w) and width (l_w), relative to the total projected length which includes the straight segments as well. As such, we model the nonlinear stretching behavior of the hyperelastic fiber element as the superposition of the stretching of the straight and wavy segments. First, the axial stiffness of the straight portion under applied force (F_e) is represented by a Mooney–Rivlin model as^[20]

$$\frac{F_e}{A_e C_1} = \left(1 + \frac{\mu_2}{\mu_1} \frac{1}{\lambda_{e,s}} \right) \left(\lambda_{e,s} - \frac{1}{\lambda_{e,s}^2} \right) \quad (1)$$

where μ_1 and μ_2 are material constants, A_e is the original cross-sectional area of the printed fiber, and $\lambda_{e,s}$ is the element extension. The extension displacement due to stretching is therefore given as

$$\delta_{e,s} = l_e (\lambda_{e,s} - 1) \quad (2)$$

On the other hand, the extension displacement due to bending (i.e., straightening) of the wavy segment is

$$\delta_{e,b} = 4 \times \left\{ h_w^2 + \left(\frac{l_w}{2} \right)^2 \right\}^{1/2} \left[\cos \theta - \cos \left(\arctan \frac{2h_w}{l_w} \right) \right] \quad (3)$$

where θ is wave angle under tensile force of F_e , determined by the equilibrium of moments as

$$dF_e \left\{ h_w^2 + \left(\frac{l_w}{2} \right)^2 \right\}^{1/2} \sin \theta \cong -K' d\theta \quad (4)$$

Here, we assume the bending stiffness of the wave is constant and given as K' . The total extension displacement δ_e is the summation of $\delta_{e,s}$ and $\delta_{e,b}$. (A detailed derivation of above equations are described in the Supporting Information). Thus, compared to tensile loading of a straight segment only (Figure 2B), the wavy element exhibits a transition between low stiffness (dominated by “opening” of the waves) at small strain to higher stiffness at large strain (dominated by stretching). The transition between bending- and stretching-dominated response is also coincident with a maximum stiffness (Figure 2C). In Figure 2E,F, the estimated force–strain and stiffness–strain

curves of the two-wave element are compared to measurements on printed samples. By changing the wave amplitude with all other parameters unchanged, we tailor the strain (in terms of percent elongation relative to the original projected length) at which the highest stiffness occurs, to above 40%.

To control the small strain stiffness we vary the extent of bonding between adjacent elements, which is simply accomplished by printing adjacent elements in contact or with a small lateral gap. Printing adjacent elements in contact causes the elements to become welded, thereby effectively increasing their thickness perpendicular to the direction of strain.^[21] The small strain stiffness depends on the bending stiffness of the waves and the bending stiffness increases in a nonlinear manner with the thickness of the fiber. As a demonstration, in Figure 2G,H we study example units containing five parallel, wavy fiber elements; in one instance all five elements are printed with lateral gaps; in another, the three central fibers are bonded; and, in the final instance, all five fibers are bonded. When all fibers are bonded the stiffness is relatively constant around 110 N m^{-1} , while when all fibers are unbonded the stiffness is 20 N m^{-1} until 10% strain, at which point it rises to a maximum of 207 N m^{-1} at 40% strain. The samples where three fibers are bonded feature intermediate stiffness values of 53 N m^{-1} at 10% strain rising to 150 N m^{-1} at 40% strain.

Also, importantly the tensile behavior of the printed thermo-plastic elastomer is resilient under cyclic loading and therefore the printed mesh elements can withstand repeated stretching and release. For instance, we found no perceptible change in the tensile response of wavy elements over 1800 cycles, to a peak strain of 32% (Figure S1, Supporting Information). Furthermore, the fiber bending stiffness, and therefore the low-strain stiffness, depends in a nonlinear manner on fiber diameter. Therefore, if the fiber becomes large enough, the bending stiffness will become similar to the stretching stiffness and the nonlinear tensile behavior will no longer be observed.

This simple design allows the digital printing of mesh designs with mechanical behavior that both qualitatively and quantitatively emulates the anisotropic, nonlinear elasticity of natural tissue. For instance, by tailoring the small strain and high strain stiffness as well as the transition strain, we show printed elastomer mesh matching the tensile response of rat muscle tissue, in both orthogonal directions (Figure 3A,B).^[22]

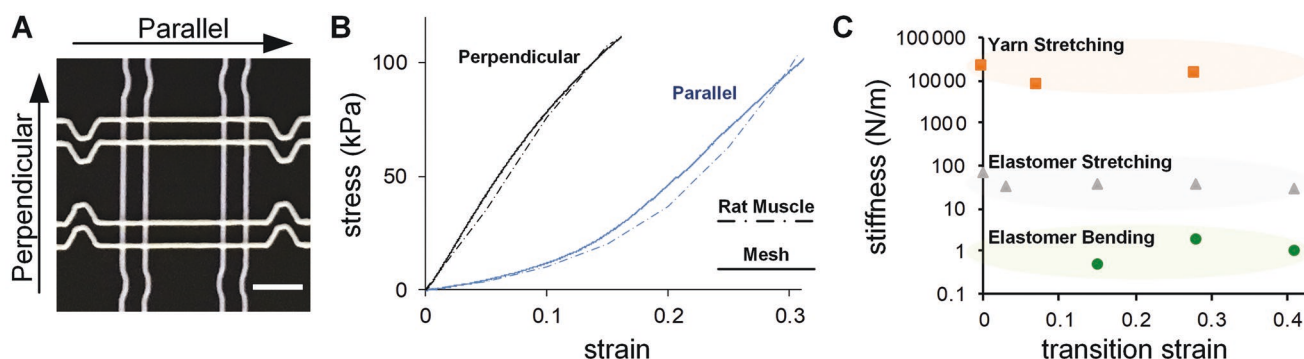


Figure 3. Tailoring mesh mechanics to match tissue. A) image (scale bar 4 mm) and B) stress strain data of a mesh unit cell (solid line) whose tensile response in two directions emulates that of muscle tissue as measured by Takaza et al.^[22] (dashed line). C) Range of stiffness and transition strains achieved by varying material composition and geometry in the mesh. The stiffness is measured as the approximately linear region before or after the transition from bending to stretching. Yarn stretching refers to incorporation of synthetic fiber, as in Figure 5.

In the direction perpendicular to the muscle fibril orientation, the mesh exhibits a relatively constant modulus of 685 kPa, while parallel to the muscle fibrils the mesh features a modulus of 111 kPa until a strain of 10% and beyond 20% strain the modulus increases to 453 kPa. Here, we applied a strain rate of 0.05 min^{-1} , which was identical to that used by Takaza et al.^[22] for their tissue measurements.

Altogether, by the strategies described herein, printed unit cells can have tensile stiffness values spanning five orders of magnitude (Figure 3C), from 20 kN m^{-1} to 0.5 N m^{-1} , and, by controlling the geometry and connectivity of the fiber elements, the transition strain can be tuned as well. The highest stiffness is achieved by incorporating continuous fiber such as stainless steel wire into the mesh, as discussed in detail later.

2.2. A Mesh-Reinforced Brace to Prevent Ankle Inversion

As a demonstration of a potential application of the nonlinear, muscle-like mechanics of the printed mesh, we built a prototype brace to selectively reinforce the inversion stiffness of the human ankle while leaving it otherwise free to move naturally. Ankle inversion is one of the most common injuries in humans and often leads to residual problems such as ankle instability and pain, especially after recurring sprains.^[23–26] As a result, soft or semi-rigid ankle braces (typically made of lycra/neoprene or nylon/polyester, respectively) are often used to prevent recurrent injuries after a mild/moderate ankle sprain.^[27] However, these devices typically uncomfortably restrict most or all of the degrees of freedom of the ankle, which limits their use by patients, can cause muscle to atrophy leading to increased susceptibility to future injury, and also negatively affects sports performance.^[28,29]

Ankle braces that are anatomically customized, either directly to the patient or made in a variety of shapes and sizes, and having locally defined, nonlinear, mechanics, could both restrict excessive motion in undesired directions (e.g., inversion) and ideally enable natural motion in other directions. We thus prototyped a device to selectively stiffen the ankle when it undergoes inversion (Figure 4A), including a strip of printed mesh placed on the outside of the ankle, such that it will experience tension when the ankle attempts to invert. Importantly, the extensibility and transition strain of the mesh were designed to allow a degree of inversion while stiffening significantly once this is exceeded. A brace was fabricated by fastening the mesh to an assembly of 3D printed components, enabling it to be fitted around a shoe and interfaced with the instrumented measurement device. This setup ensured a rigid attachment to the body and that the forces were transferred via the nonlinear mesh. Finally, the wavy component of the mesh (which has the nonlinear tensile response) is layered without bonding, to make it flexible in bending out of plane and therefore allowing it to buckle, so that it does not affect the stiffness in eversion.

We then measured the static component of multivariable ankle mechanical impedance, a generalization of ankle stiffness, with and without the mesh placed over the ankle joint. Using an Anklebot (Bionik Laboratories Corporation, Watertown, MA), the static torque–angle relation in the inversion/eversion (IE) and dorsiflexion/plantarflexion (DP) directions

were simultaneously measured and used to estimate ankle stiffness in different directions within IE-DP space.^[23]

Data from four subjects indicate that our brace is able to selectively increase the linear approximation of effective ankle stiffness in inversion while leaving it relatively unaffected in other directions (Figure 4C,D and Figure S4, Supporting Information). Across all four subjects, wearing the mesh increased the effective ankle stiffness by an average of 78.69% in the inversion direction and only by 14.27% in eversion, -1.59% in dorsiflexion, and -1.40% in plantarflexion. Moreover, the results show that the added stiffness is nonlinear (Figure 4D and Figure S4, Supporting Information). The torque required to achieve angular displacement in inversion is relatively similar whether or not a brace is worn up to $\approx 1.5^\circ$, after which the stiffness of the ankle with the brace becomes steadily higher until it is $\approx 50\%$ greater than that of the bare ankle at an inversion of 15° . These results suggest that meshes with nonlinear tensile response are promising candidates for making future braces that only prevent motion that will lead to injury, while otherwise leaving the ankle to move freely. Such braces may have significant potential both as prophylactic braces as well as aiding rehabilitation by enabling patients to resume activities more quickly.

2.3. Printing Fiber-Reinforced Mesh

Thermoplastic elastomer meshes can achieve widely tailored mechanical properties for use in devices such as the ankle brace described above. However, many potential applications of printed mesh—including implantable hernia mesh—will demand greater stiffness and strength. Specifically, the stiffness of a strained elastomer mesh depends on the cross-sectional area of its fibers and therefore is proportional to the amount of printed material. However, to treat injury of some connective tissues an even greater stiffness is needed in the large strain regime, preventing excessive deformations and, ultimately, failure; for contrast, see Figure S2a in the Supporting Information where one all-elastomer unit cell breaks at 2.4 N.

A strategy to digitally fabricate stronger mesh is to incorporate synthetic fibers or threads into the printing process. AM of fiber-reinforced components is well known, particularly via placing a thermoplastic-coated thread into the layers of 3D components such as mechanical fixtures and brackets.^[30] While this gives components with significantly enhanced flexural rigidity and strength, for printing mesh it is desirable to leave the fiber unconstrained in the open areas of each unit cell, to enable it to become taut only at a critical strain where the highest stiffness is needed. In other words, a continuous fiber such as a fine metal wire is compliant in bending like printed thermoplastic filament, but much more rigid in tension.

To incorporate continuous fiber into mesh, we implement a second (unheated) nozzle on the extrusion 3D printer, and thread the fiber through the nozzle. This allows the deposition of continuous fiber without a thermoplastic sheath by instead using an adhesive substrate to passively pull fiber out of a nozzle (Figure 5B,C and Video S1, Supporting Information). We place a film with adhesive on both sides onto the printer bed and then extrude a layer of thermoplastic onto this, according

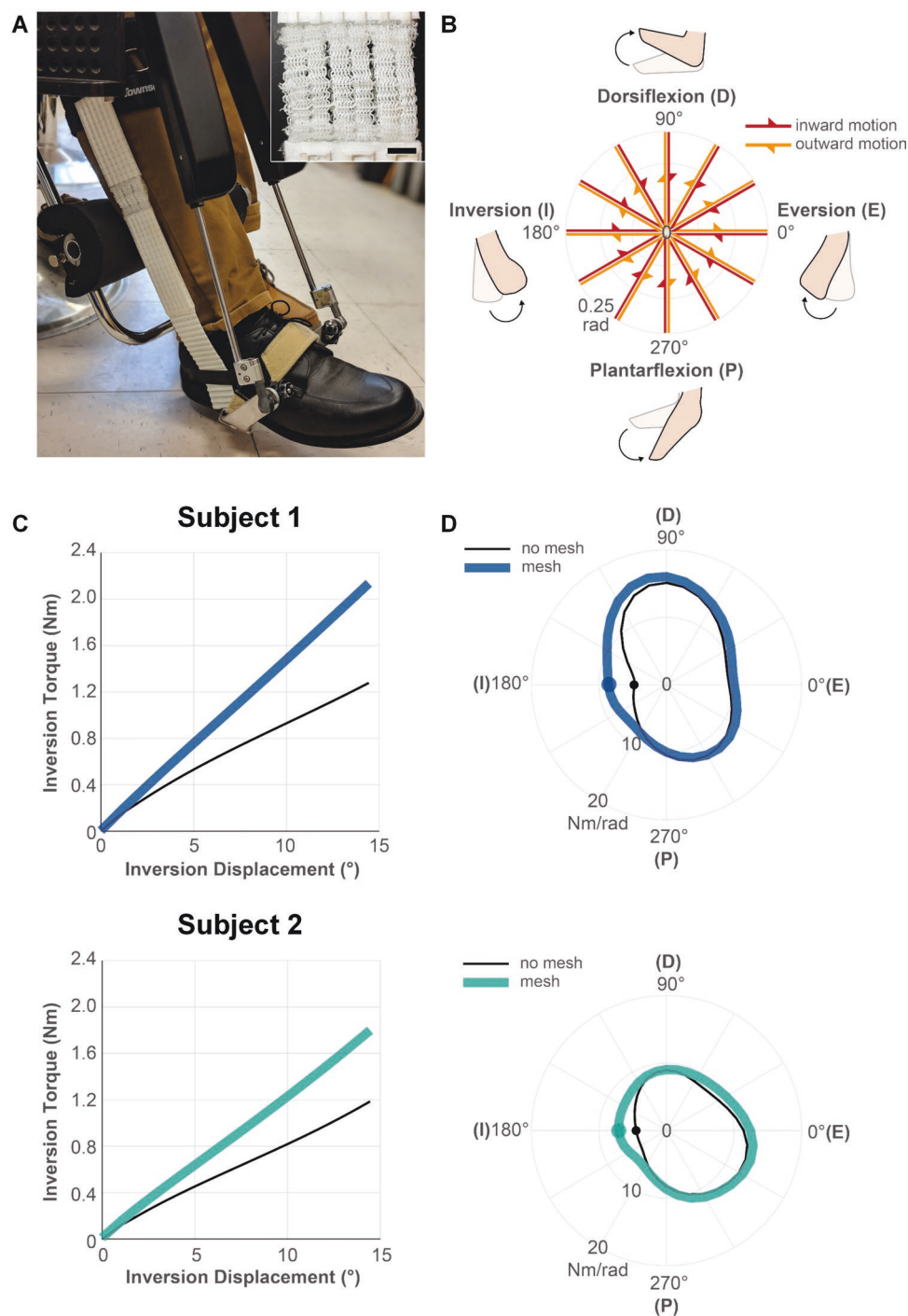


Figure 4. Demonstration of digitally tailored mesh for resisting ankle inversion. A) A nonlinear mesh incorporated into an ankle brace and the attachment of this brace to the robot used for ankle stiffness measurement. Inset shows the mesh portion of the brace (scale bar 10 mm). B) Schematic showing the 12 directions the ankle is rotated in in order to generate the stiffness measurements. C) Plots of the torque versus angular displacement in inversion for two human subjects. D) Stiffness distribution in the ankle of these two subjects, with and without the mesh device.

to the thermoplastic mesh design but leaving gaps where continuous fiber is desired. We move the fiber nozzle over the substrate, causing the fiber to follow the path of the nozzle and stick to the adhesive. The continuous fiber is patterned such that it overlaps with the already extruded thermoplastic in some regions. In order to bond the fiber to the rest of the mesh, we

deposit another layer of thermoplastic in an identical pattern to the first layer, which sandwiches the fiber. Here, we print stainless steel thread as the continuous fiber, which is impervious to the temperatures used for thermoplastic extrusion ($\approx 210^\circ\text{C}$). Many other fiber materials with suitable thermal stability could be used, such as carbon fiber and Kevlar.

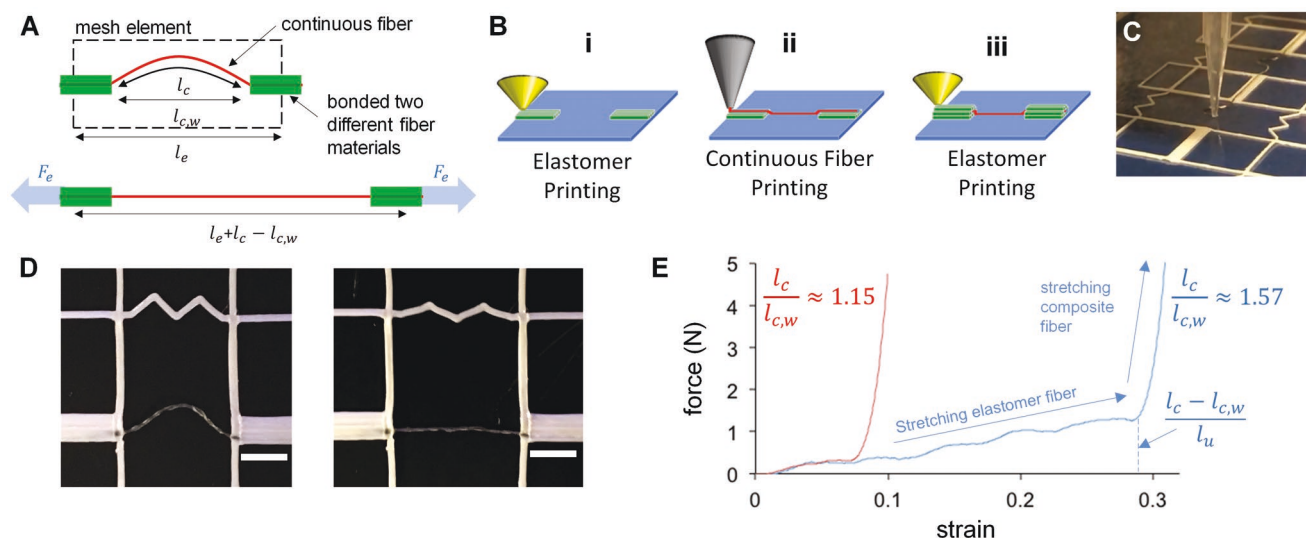


Figure 5. Reinforcing digitally tailored mesh using continuous fiber. A) Schematic showing how a stainless steel thread is placed within the bonded elastomer mesh, with a free length of slack. B) Method of patterning continuous fiber mechanism including sandwiching between extruded layers. C) Image of fiber printing. D) Image of unit cell with continuous fiber (scale bar 4 mm), unstretched (left) and stretched (right). E) Force–strain curves for two exemplary fiber-reinforced mesh samples, with different initial slack, where l_u denotes the unit cell length (smoothed with Savitzky–Golay filter).

Here, a mesh that permits a continuous toolpath is important to minimize need to cut the fiber. And, because the continuous fiber cannot change direction unless it is in contact with the adhesive substrate, the fiber nozzle must be very close to the print bed for accurate patterning. Also, the cell must have a minimum curvature due to the forces that build up in the fiber during bending. Finally, there has to be overlap between continuous fiber and elastomeric matrix to allow the continuous fiber to be bonded to the mesh. Taking these into consideration, we designed the unit cell shown in Figure 5D for use with continuous fiber.

These unit cells exhibit greater large strain stiffness than is possible with the all-elastomer designs, while retaining a large open area. In particular, the tensile response (Figure 5E) of these unit cells is governed by the elastomer at small strains (180 N m^{-1} stiffness), and stiffens sharply when the steel fiber becomes taut (7.3 kN m^{-1}). As with the all-elastomer unit cells, the strain at which this transition occurs can be controlled by the wave amplitude of the premade fiber, and the large strain stiffness is governed by the fiber properties. The ultimate strength depends on the mesh design and the continuity of fiber path but can be limited by the fiber-polymer adhesive strength.

2.4. Toward Conformal, Customized Mesh-Based Assistive Devices

Looking forward to broader uses of digitally tailored mesh in wearable and implantable devices, another important capability is conformality to 3D surfaces, both for increased comfort as well as to controllably transfer mechanical forces. This will ultimately be achieved by more sophisticated planning algorithms that relate the desired shape and mechanics to the mesh topology, and plan the printer toolpath accordingly including via nonplanar printing layers.^[31] Toward this goal, we show three further capabilities: 1) controlling drape by modulating

bonding between orthogonal filaments; 2) coupling in-plane and out-of-plane displacements via mesh cells with negative Poisson's ratio; and 3) printing mesh onto 3D templates.

Conventional textiles are highly conformable because the constituent fibers (both within individual threads and yarn, and within knits and weaves) can slip over one another. It was explained earlier that slip is undesirable for precise control of in-plane stress and strain; however, it can be useful if placed locally to allow mesh conformality. In the printing process, we therefore locally enable fiber slip by lifting the printer nozzle as it passes over filament in the mesh, such that the newly printed filament cools before it contacts the underlying filament on the print bed (Figure 6A). Printing fibers that are not bonded significantly enhances the drape of an exemplary printed fabric. Comparing two otherwise identical specimens placed in a cantilever configuration, the unbonded fabric deflects vertically $\approx 230\%$ more than the bonded fabric. Over a sphere (here, a golf ball), the unbonded fabric wraps the sphere while the bonded one does not. Control of the Poisson's ratio at the unit cell-level can also allow the fabric to conform to a curved surface without folding.^[32] As a demonstration, a printed mesh with locally negative Poisson's ratio is placed onto the author's knee (Figure 6B).^[33] When the same mesh is stretched in-plane by hand, it can bulge upward (Video S1, Supporting Information), suggesting that inverse design of the mesh pattern can enable complex strain profiles to be followed.

Last, explicit control of the printing toolpath also enables the production of nonplanar meshes (Figure 6C), providing another means for devices to conform to the body while maintaining the desired mechanics for biomechanical reinforcement. To print mesh for a glove-like brace on a hand, we first 3D print support structure designed to approximate the height and position of a knuckle. Next, we cover these knuckle templates with tape to prevent the extruded mesh from adhering to the support directly. A graph-theory based, algorithm

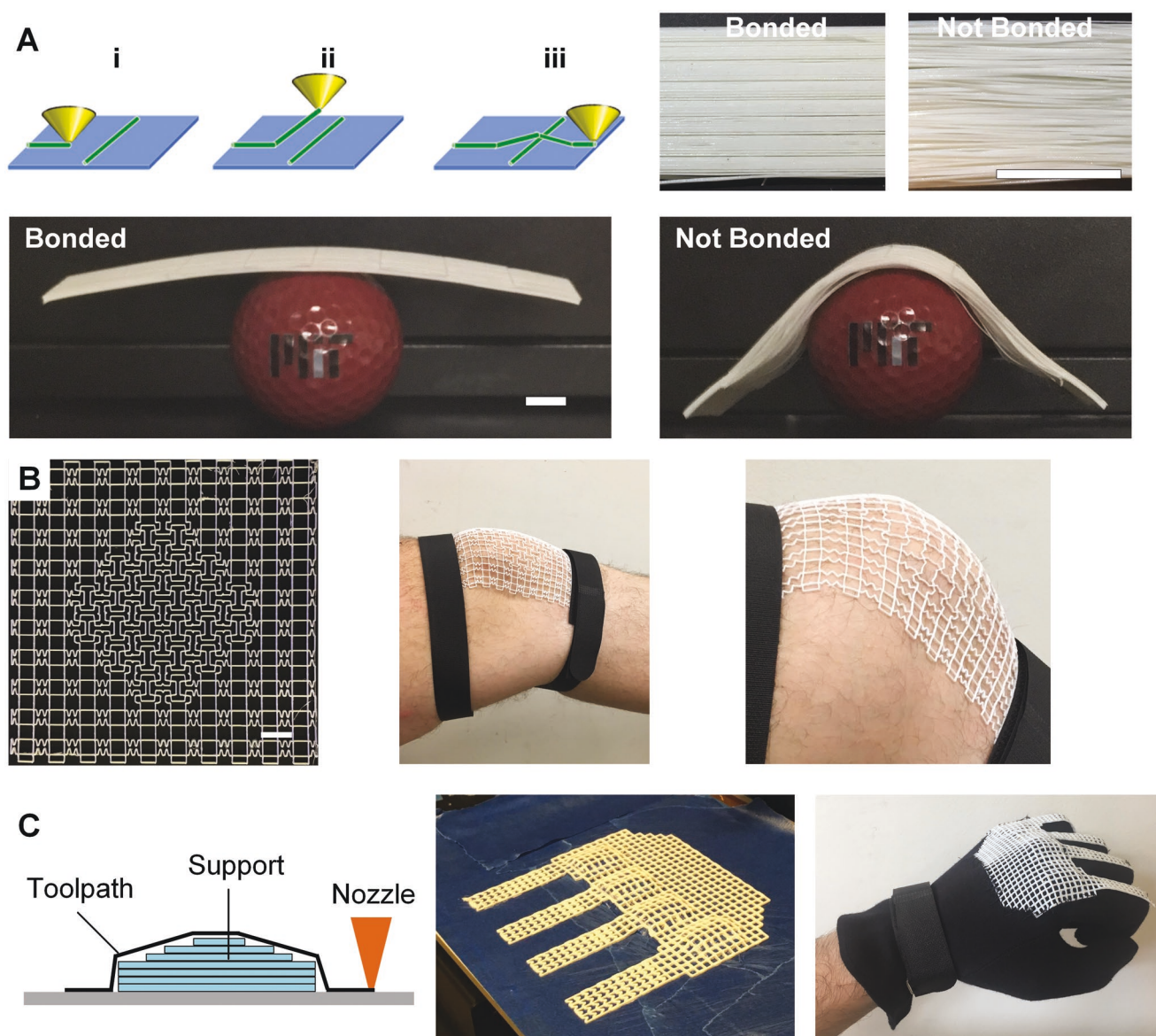


Figure 6. Additional capabilities of mesh printing. A) Modulation of fiber–fiber bonding using 3D toolpaths that allow the fiber to cool before it touches the previous, orthogonally placed fiber. This results in the nonbonded swatch having noticeably greater drape (scale bar 10 mm). Trademarked MIT logo reproduced with permission. B) A mesh (scale bar 10 mm) with locally patterned negative Poisson's ratio unit cells, which featuring anisotropic mechanics and showing its ability to conform to a knee. C) Printing of conformal mesh onto a template, and after which the mesh is sewn onto a glove. This mesh-enhanced glove exerts a restoring force on the fingers when the fist is clenched, as is commonly necessary in stroke rehabilitation.

developed in a separate study, is used to plan the toolpath over the prescribed boundary and curved topography, with a minimum number of discontinuities.^[18] The mesh is then sewn to a glove, and is therefore designed to counteract spasticity (increased stiffness) by providing extension forces to a clenched fist, which can occur from neurological injuries such as acute ischemic stroke.^[34]

3. Conclusion

We have demonstrated a route to digital tailoring of compliant mesh materials, which may find wide application in the design

and manufacturing of wearable and implantable devices. Importantly, the printed mesh architecture enables engineered nonlinear mechanics that can mimic those of soft tissue and enable 3D conformality to the body. We demonstrate a process where explicit control of the printer toolpath, a hierarchical mesh design, and new hardware for patterning of continuous fibers enables the additive manufacture of parts with locally controlled mechanics matching those of individuals' soft tissue. Moreover, we demonstrate how our toolpath software enables the production of meshes with 3D structure that allows better conformability to the body through interfiber bonding control for improved drape, locally patterned negative Poisson's Ratio regions, and 3D toolpaths printed onto support structures. We

produce an example ankle brace that shows the potential of controlled nonlinear tensile response by letting the ankle move freely unless it inverts to an excessive extent as well as a glove with an embedded mesh designed to conform to the hand. Inverse design of meshes, where mesh material and geometry are designed to generate desired properties would enable unprecedented novel devices that seamlessly interact with the body, and thereby improve the lives of countless patients suffering from conditions ranging from ankle or other joint sprain to hernia and tremors.

4. Experimental Section

Printing: Extrusion is done using a commercial 3D printer Printbot Simple Metal. Thermoplastic Polyurethane (Ninjaflex) is the primary matrix material used, while stainless steel thread (0.4 mm thick 3 ply thread, 316 L alloy, Adafruit Industries) is the premade continuous fiber. For continuous fiber deposition, the substrate is made adhesive through the use of double-sided tape. The nozzle used to guide the continuous fiber is a tapered nozzle from Nordson (product number). A holder was printed for the nozzle to sit next to the extruder as shown in Figure S1 in the Supporting Information.

Toolpath Planning: The toolpath is essential to achieving the best mechanics/morphology from the fabrics and therefore their own software was written in the Python language to do this. The software takes as input the desired array of unit cells in the mesh alongside printing parameters such as rate and temperature and translates these into g-code, which are the instructions for the printer. The g-code output by the Python software is then input into Repetier-Host software as manual g-code, which passes the instructions to the printer.

Mechanical Testing: Tensile testing was conducted using an Instron 1125 machine with a 20 000 lb. (2511-305) and a 100 N load cell (Omega S-type). All tests were conducted taking 3000 data points per minute at a displacement rate of 5 mm min⁻¹. Flexural testing was carried out by attaching a mass to fibers or fabrics and measuring the vertical displacement.

Finite Element Modeling: For the modeling of individual fibers, a finite element formulation based on the so-called geometrically exact Simo–Reissner beam theory, incorporating the deformation modes of axial tension, shear, torsion,^[35] and bending, has been applied. The formulation is geometrically nonlinear and accounts for arbitrarily large displacements and rotations as well as for finite strains. The stress–strain relationship is based on an elastic constitutive law defined by Young's modulus and Poisson's ratio. All simulations have been conducted in a quasi-static manner employing the in-house finite element research code BACI developed at the Institute for Computational Mechanics at the Technical University of Munich.^[36]

Ankle Measurements Experimental Setup: Four subjects (age: 27±4 years; gender: three male, one female) with no reported history of biomechanical or neuromuscular disorders participated in the experiment. All gave informed written consent before the experiment. The experimental protocol was reviewed and approved by the Institutional Review Board of the Massachusetts Institute of Technology. Subjects wore a modified shoe and a knee brace on their right leg, to which the Anklebot was attached.^[37] The knee brace was attached to the chair such that weight of the robot and leg were fully supported and the foot did not contact the ground (Figure 4A). Subjects were instructed to remain relaxed during the experiment.

Each trial consisted of 24 movements (an inward and outward motion along 12 equally spaced directions in IE-DP space, with a nominal displacement amplitude of 15° in each direction at constant speed of 5° s⁻¹) (Figure 4B). The robot speed was selected to maintain a quasi-static relationship between measured torque and displacement and avoid evoking spindle-mediated stretch reflexes. For each movement, the robot moved the ankle along a commanded trajectory and recorded

applied torque and actual angular displacement at 200 Hz sampling frequency.

Four trials were conducted in each of two conditions: *no mesh* and *mesh*. During trials in the *mesh* condition, one end of the mesh was attached to the knee brace and the other was attached to the shoe on the lateral side of shank, parallel to the tibia (Figure 4A).

Ankle Measurement Data Analysis: In each condition, a vector field, V , defined as

$$(\tau_{IE}, \tau_{DP}) = V(\theta_{IE}, \theta_{DP}) \quad (5)$$

was approximated from measured multivariable torque–angle relation in IE-DP space for each individual subject. θ_{IE} and θ_{DP} are the angular displacements in the IE and DP directions, respectively, and τ_{IE} and τ_{DP} are the corresponding applied torques. Figure 4C shows 2D slices of the two vector fields (*mesh* and *no mesh*) in the inversion direction for two example subjects. As expected, the mesh added nonlinear stiffness to the ankle.

To evaluate the directional effect of the mesh, ankle stiffness was also evaluated for all directions in each condition (*mesh* and *no mesh*). Ankle stiffness for a given direction was calculated as the slope of a linear approximation of the vector field in that direction.

Supporting Information

Supporting Information is available from the Wiley Online Library or from the author.

Acknowledgements

Financial support was provided by a National Science Foundation Science, Engineering, and Education for Sustainability postdoctoral fellowship (Award No.: 1415129) to S.W.P.; a Samsung Scholarship to J.L.; the MIT-Skoltech Next Generation Program to A.J.H. and S.W.P. the School of Engineering and Sciences from Tecnológico de Monterrey to R.R.; the Manufacturing Demonstration Facility, Oak Ridge National Laboratory, the Department of Energy, UT-Batelle, Oak Ridge Associated Universities, the DOE's Advanced Manufacturing Office to (for G.D.); the German Academic Exchange Service (Deutscher Akademischer Austauschdienst) to C.M.; and the Eric P. and Evelyn E. Newman Fund and NSF-CRCNS-1724135 to N.H. The authors would also like to acknowledge helpful discussions with Adam Stevens and Abhinav Rao. S.W.P. and A.J.H. are inventors on an MIT patent application: Systems, Devices, and Methods for Extrusion-Based Three-Dimensional Printing. U.S. Ser. No. 15/376,416. PCT Ser. No. PCT/US16/66205. This application primarily addresses the printing process for the mesh. S.W.P., A.J.H., M.E.H., J.L., and R.R. are also inventors on an MIT provisional patent application: Additively Manufactured Mesh Materials, Wearable and Implantable Devices, and Systems and Methods for Manufacturing the Same, U.S. Ser. No. 62/797,044. This application primarily addresses applications for the mesh.

Conflict of Interest

The authors declare no conflict of interest.

Keywords

additive manufacturing, biomechanics, medical devices

Received: March 1, 2019

Revised: April 16, 2019

Published online: June 19, 2019

- [1] S. Patra, V. Young, *Cell Biochem. Biophys.* **2016**, 74, 93.
- [2] S. L. Sing, J. An, W. Y. Yeong, F. E. Wiria, *J. Orthop. Res.* **2016**, 34, 369.
- [3] M. Martorelli, S. Gerbino, M. Giudice, P. Ausiello, *Dent. Mater.* **2013**, 29, e1.
- [4] R. Trombetta, J. A. Inzana, E. M. Schwarz, S. L. Kates, H. A. Awad, *Ann. Biomed. Eng.* **2017**, 45, 23.
- [5] Y. He, G. Xue, J. Fu, *Sci. Rep.* **2015**, 4, 6937.
- [6] P. P. Pott, M. L. R. Schwarz, R. Gundling, K. Nowak, P. Hohenberger, E. D. Roessner, *PLoS One* **2012**, 7, 1.
- [7] A. Kingsnorth, K. LeBlanc, *Lancet* **2003**, 362, 1561.
- [8] K. Junge, U. Klinge, A. Prescher, P. Giboni, M. Niewiera, V. Schumpelick, *Hernia* **2001**, 5, 113.
- [9] B. Calvo, A. Ramirez, A. Alonso, J. Grasa, F. Soteras, R. Osta, M. J. Munoz, *J. Biomech.* **2010**, 43, 318.
- [10] M. Śmietarski, K. Bury, A. Tomaszewska, I. Lubowiecka, C. Szymczak, *Surg. Endosc. Other Interv. Tech.* **2012**, 26, 1461.
- [11] J. Mccann, L. Albaugh, V. Narayanan, A. Grow, W. Matusik, J. Mankoff, J. Hodgins, *ACM Transactions on Graphics* **2016**, 35, 49.
- [12] B. Bickel, B. Bäcker, M. A. Otaduy, H. R. Lee, H. Pfister, M. Gross, W. Matusik, *ACM Transactions on Graphics* **2010**, 29, 63.
- [13] M. Akbari, A. Tamayol, S. Bagherifard, L. Serex, P. Mostafalu, N. Faramarzi, M. H. Mohammadi, A. Khademhosseini, *Adv. Healthcare Mater.* **2016**, 5, 751.
- [14] A. Johnson, G. A. Bingham, D. I. Wimpenny, *Rapid Prototyping J.* **2013**, 19, 199.
- [15] J. White, M. Foley, A. Rowley, *3D Print. Addit. Manuf.* **2015**, 2, 145.
- [16] H. Peng, J. Mankoff, S. E. Hudson, J. Mccann, in *Proceedings of the 33rd Annual ACM Conference on Human Factors in Computing Systems*, ACM, New York **2015**, 1789.
- [17] P. Bettini, G. Alitta, G. Sala, L. Di Landro, *J. Mater. Eng. Perform.* **2017**, 26, 843.
- [18] G. Dreifus, K. Goodrick, S. Giles, M. Patel, R. M. Foster, C. Williams, J. Lindahl, B. Post, A. Roschli, L. Love, V. Kunc, *3D Print. Addit. Manuf.* **2017**, 4, 98.
- [19] T. Ushiki, *Arch. Histol. Cytol.* **2002**, 65, 109.
- [20] A. Bower, *Applied Mechanics of Solids*, CRC Press, Boca Raton, Florida, USA **2009**.
- [21] J. E. Seppala, S. Hoon Han, K. E. Hillgartner, C. S. Davis, K. B. Migler, *Soft Matter* **2017**, 13, 6761.
- [22] M. Takaza, K. M. Moerman, J. Gindre, G. Lyons, C. K. Simms, *J. Mech. Behav. Biomed. Mater.* **2012**, 17, 209.
- [23] C. Doherty, E. Delahunt, B. Caulfield, J. Hertel, J. Ryan, C. Bleakley, *Sports Med.* **2014**, 44, 123.
- [24] L. Tanen, C. L. Docherty, B. Van Der Pol, J. Simon, J. Schrader, *Foot Ankle Spec.* **2014**, 7, 37.
- [25] J. P. Gerber, G. N. Williams, C. R. Scoville, R. A. Arciero, D. C. Taylor, *Foot Ankle Int.* **1998**, 19, 653.
- [26] M. S. Yeung, K. M. Chan, C. H. So, W. Y. Yuan, *Br. J. Sports Med.* **1994**, 28, 112.
- [27] E. Eils, C. Demming, G. Kollmeier, L. Thorwesten, K. Völker, D. Rosenbaum, *Clin. Biomech.* **2002**, 17, 526.
- [28] L. Deberg, M. T. Andani, M. Hosseinipour, M. Elahinia, *Smart Mater. Res.* **2014**, 2014, 572094.
- [29] K. Tamura, K. N. Radzak, R. E. Vogelpohl, B. A. Wisthoff, Y. Oba, R. K. Hetzler, C. D. Stickley, *Gait Posture* **2017**, 58, 108.
- [30] R. Matsuzaki, M. Ueda, M. Namiki, T.-K. Jeong, H. Asahara, K. Horiguchi, T. Nakamura, A. Todoroki, Y. Hirano, *Sci. Rep.* **2016**, 6, 23058.
- [31] R. J. A. Allen, R. S. Trask, *Addit. Manuf.* **2015**, 8, 78.
- [32] M. Konakovic, J. Panetta, K. Crane, M. Pauly, *ACM Trans. Graphics* **2018**, 37, 1.
- [33] A. Clausen, F. Wang, J. S. Jensen, O. Sigmund, J. A. Lewis, *Adv. Mater.* **2015**, 27, 5523.
- [34] P. P. Urban, T. Wolf, M. Uebele, J. J. Marx, T. Vogt, P. Stoeter, T. Bauermann, C. Weibrich, G. D. Vucurevic, A. Schneider, J. Wissel, *Stroke* **2010**, 41, 2016.
- [35] C. Meier, A. Popp, W. A. Wall, *Arch. Comput. Meth. Eng.* **2019**, 26, 163.
- [36] W. A. Wall, A. Popp, M. Kronbichler, A. Mayr, C. Meier, A.-T. Vuong, C. Ager, F. Bräu, M. J. Grill, *BACI: A Multiphysics Simulation Environment*, Technical University of Munich, Munich, **2019**.
- [37] H. Lee, P. Ho, M. A. Rastgaar, H. I. Krebs, N. Hogan, *J. Biomech.* **2011**, 44, 1901.